UNSTEADY AND POST-STALL AERODYNAMIC MODELING FOR AIRCRAFT DYNAMICS SIMULATION

Ryan C. Paul[1], Joseba Murua[2], and Ashok Gopalarathnam[1]

[1]North Carolina State University, Department of Mechanical and Aerospace Engineering, EB 3, 911 Oval Drive, Raleigh, NC 27695-7910, rcpaul@ncsu.edu, agopalar@ncsu.edu

[2]Pilatus Aircraft Ltd, P.O. Box 992, 6371 Stans, Switzerland, jmurua@pilatus-aircraft.com

Keywords: vortex lattice method, unsteady aerodynamics, potential flow, flight dynamics, stall

Abstract: By extending an unsteady vortex lattice method with a decambering approach to handle stall, a modeling environment has been developed for flight dynamics analysis of rigid aircraft in pre- and post-stall conditions, with possible future extensions to include structural flexibility. The combined equations for vortex-lattice analysis, rigid-body flight dynamics, and decambering stall model are integrated for semi-analytical analysis of the coupled system. The resulting framework allows for performing aircraft-trim calculations in both pre-stall and post-stall conditions. Linearization about the trim condition leads to a state-space form, with states including vortex-lattice and flight-dynamic variables. The decambering variable for each section is introduced in the system matrices as a control variable, whose value is linearly related to the changes in flight velocities. Eigenvalue analysis of the resulting system matrix yields the flight dynamic modes. Results for loss of roll damping with increase in angle of attack beyond stall show excellent agreement with high-alpha data from flight-test results in the literature. Full-aircraft results for all flight modes are verified for pre-stall conditions. At post-stall conditions, the full-aircraft predictions for some modes are in broad agreement with the limited general trends that could be found in the literature.

1 Introduction

The current state of the art in analysis, simulation, and control of flight dynamics of flexible aircraft relies mostly on low-order models for the description of aerodynamic loads [1, 2, 3, 4]. These low-order aerodynamic models are often founded in potential-flow theory, and are therefore limited to unstalled flows, or use simplified stall models, in which the aerodynamic interactions between the stalled and non-stalled portions of the partially-stalled wings is not considered [5, 6]. Approaches to analyze the flight dynamics of moderate-to-high aspect ratio flexible aircraft require the modeling of the interactions between unsteady aerodynamics of lifting surfaces of an aircraft including the effects of stall, flight dynamics, and effects of flexibility. As a step toward this bigger objective, the current effort focuses on the interactions between the first two elements: unsteady aerodynamics including stall and flight dynamics. The underlying framework, however, is capable of handling structural flexibility, which will be included in a follow-on effort.

At the foundation for the current work, is the framework of the Simulation for High Aspect Ratio Planes (SHARP) [4] code, which utilizes an unsteady vortex lattice method

(UVLM) for potential flow in conjunction with a nonlinear beam model to simulate flexible aircraft flight dynamics. The structure is assumed to be rigid in the current work. While SHARP has been shown to be accurate in attached flow [4, 7], it does not account for stall, a regime approached in large gust encounters or aggressive maneuvers. This paper presents the incorporation of post-stall modeling into SHARP using decambering, and investigates its effect on aircraft trim and flight-dynamics stability, with the assumption of rigid structures.

The paper will begin by describing the integration of a static-stall model into SHARP. A number of research efforts have studied the incorporation of stall effects in low-order aerodynamic theories for finite wings using the nonlinear lift curves for the airfoil sections as inputs. The stall model in this paper uses the decambering approach developed at NC State University [8, 9], in which airfoil aerodynamic-coefficient information for all spanwise strips across all wings is provided as input. Each strip is given a decambering variable, which is essentially a rotation of strip normal vectors, to account for the effects of boundary-layer separation. The input C_l-α information for the sections is used in determining the convergence of the decambering variables during aerodynamic load calculation. Pre-stall, no decambering is necessary. Post-stall, initial aerodynamic load evaluation is carried out using the UVLM. As the corresponding sectional operating points $(\alpha(i), C_l(i))$ will not fall on the input curves, decambering variables are modified iteratively to bring the operating points onto the viscous data while simultaneously satisfying the boundary conditions of the UVLM.

The post-stall capabilities will be first presented by performing aircraft trim in both pre- and post-stall cases for a representative unmanned configuration. Next, linearization of the aircraft dynamics equations is carried out about trim conditions, leading to a state-space system of the form $\dot{x} = Ax$, where x includes aerodynamic and rigid-body states, as well as elastic ones if required. The eigenvalue analysis of the system yields the flight dynamics modes of the vehicle, and could capture couplings with structural modes, in the future. For post-stall flight dynamics, decambering is introduced into the system matrices by treating it at each strip as a control effector, whose deflection is linearly related to the change in flight velocities. This relationship between the change in flight velocities and change in decambering is appended to the system in feedback form, whose stability may be determined from an eigenvalue analysis of the matrix $[A - BK]$.

The paper will introduce novelties such as trimming in post-stall conditions using UVLM aerodynamics with physics-based stall modeling. The decambering approach lends itself to a natural incorporation into a framework suitable for stability analysis, and it is therefore expected to result in an efficient tool for loads and aeroelasticity in post-stall conditions.

2 Methodology

The results in this paper are based on studying configurations using a linearized version of an aeroelastics code, which combines a UVLM and nonlinear beam model, about an equilibrium condition. The aerodynamic model in the aeroelastics code is heavily modified to incorporate the effects of flow separation using an iterative decambering procedure. To provide background for the reader, this section describes the separate models. Section 2.1 covers the post-stall aerodynamic model, based on iterative decambering. Section 2.2 presents the governing equations of the aerodynamic model used in this work. Section 2.3 gives a brief background on the SHARP framework used to perform the linearization and
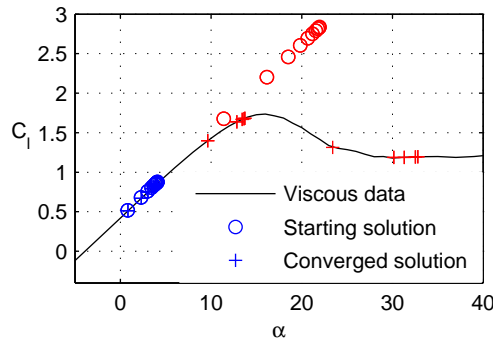
Figure 1: Decambering solution for sections of a rectangular wing with symbols showing starting and converged solutions for pre-stall (blue) and post-stall (red) angles of attack.

to predict flight dynamic modes. Finally, Section 2.4 discusses how the stall model is integrated into the framework for stability analysis.

2.1 The Decambering Post-Stall Model

This section gives a brief overview of the decambering concept as it is utilized in conjunction with a potential flow aerodynamics analysis method to model the effects of flow separation. While this discussion focuses on applying decambering to a finite wing, the idea has been applied to configurations of several lifting surfaces.

Decambering is straightforward to apply in 2D aerodynamics. The camber reduction is simply set at the required value to effectively tilt the local section such that the reduction in lift due to viscous effects is matched by the potential-flow solution. In a 3D aerodynamics analysis method, application of decambering is most easily thought of as a rotation of the normal vectors for all chordwise panels in a spanwise strip by a decambering angle, δ_1. However, finding the correct value of δ_1 for each strip on a 3D wing is not straightforward because the modification of a particular section's δ_1 is likely to have an effect on the δ_1 values of the neighboring strips and on lifting surfaces downstream of this strip. Because of the effect that changing one strip's camber has on other sections, the decambering procedure is implemented using a Newton-Raphson iteration. Hence, while the input data relies on 2D viscous curves, the approach is 3D, since the interference among all strips is accounted for until convergence is reached. Pre- and post-stall starting and converged solutions for a finite wing are shown in C_l-α space in Figure 1. The decambering procedure, as applied to the finite wing case, is described in detail in Ref. [9].

2.2 The Unsteady Vortex Lattice Method

The unsteady vortex lattice method (UVLM) is an efficient computational technique to solve 3-D potential-flow problems about moving (and deforming) lifting surfaces. The basics of the standard UVLM algorithm are described by Katz and Plotkin [10], but an alternative formulation will be used herein, following closely that presented in Ref. [4] whereby the governing equations are written in state-space form, ideally suited for flight simulation.

In the UVLM, elementary solutions are distributed over lifting surfaces and the non-penetration boundary condition is imposed at a number of control (collocation) points. The elementary solution is the so-called vortex ring, distributed over the instantaneous

mean surface, ignoring thickness. The leading segment of the vortex ring lies on the panel's quarter-chord line, and a collocation point is placed at the three-quarter-chord line, which falls at the center of the vortex ring. As the surface moves along its flight path, a force-free wake, also represented by vortex rings, is obtained as part of the solution procedure. By imposing the non-penetration boundary condition at a number of collocation points, a system of algebraic equations is obtained. Thus, at discrete time step $n + 1$, the vorticity distribution of the bound vortex elements is determined by

$$A_{cb}\mathbf{\Gamma}_b^{n+1} + A_{cw}\mathbf{\Gamma}_w^{n+1} + \boldsymbol{w}^{n+1} = 0, \tag{1}$$

where $\mathbf{\Gamma}_b$ and $\mathbf{\Gamma}_w$ are the column vectors with the circulation strengths in the bound and wake vortex-rings, respectively; $A_{cb} = A_{cb}(\boldsymbol{\zeta}_b)$ and $A_{cw} = A_{cw}(\boldsymbol{\zeta}_b, \boldsymbol{\zeta}_w)$ are the wing-wing and wing-wake aerodynamic influence coefficient matrices, computed at the collocation points through the Biot-Savart law; and $\boldsymbol{\zeta}_b$ and $\boldsymbol{\zeta}_w$ are the column vectors with the bound and wake grid coordinates. $\boldsymbol{w}$ in Eq. (1) is the column vector of normal components of all velocities except those induced by bound and wake vorticity, which may encompass deployment of control surfaces, gust induced velocities, wing deformations and rigid-body motions, and will be denoted here as "non-circulatory velocity". It also includes the contribution of the decambering, when applicable in the post-stall regime. At each time step, as the circulation of the wing changes, a new row of vortex rings will be shed into the wake from the trailing edge of each lifting surface. In addition to this, the existing wake may be displaced following the local flow velocity (*free-wake* model). An accurate description of a force-free wake might be essential when it impinges on a body, such as during wake encounters on trailing aircraft or blade-vortex interactions on rotorcraft. However, its impact on the fixed-wing-aircraft flight dynamics considered in this work has been shown to be minimal [11]. As a result, and as it is a computationally very expensive process that requires the evaluation of the local velocities at the wake grid-points, a fixed wake model was used for the current work. The propagation equations for the wake circulation can be written in discrete time as

$$\mathbf{\Gamma}_w^{n+1} = C_{\Gamma b}\mathbf{\Gamma}_b^n + C_{\Gamma w}\mathbf{\Gamma}_w^n, \tag{2}$$

where $C_{\Gamma b}$ and $C_{\Gamma w}$ map the circulation of the previous time step to the current one, and they are very sparse constant matrices which account for Kelvin's circulation theorem and Helmholtz's vortex theorem.

Once the distribution of vorticity has been obtained at each time step, the inviscid aerodynamic loads can be computed. Different methods exist, such as the expressions given by Katz and Plotkin [10], which are based on the unsteady Bernoulli equation but use the small-angle assumption and introduce an approximation for induced drag in order to account for leading edge suction.

2.3 The SHARP Toolbox

Simulation of High Aspect Ratio Planes (SHARP) [4, 12] is a medium-fidelity tool designed originally for the simulation of large, flexible aircraft. It couples an aerodynamics model, based on the UVLM, and a structural model, based on a finite-element representation of a nonlinear beam. SHARP is capable of performing both aerodynamic and aeroelastic analysis, in addition to flight-dynamic analysis for a full-aircraft configuration. Using the framework established by SHARP, full nonlinear time-marching simulations may be performed. These simulations are quite computationally expensive. A very powerful feature of SHARP, and the mode by which it is used in this work, is the ability to perform

a linearization of the aerodynamic and structural equations, resulting in a combined aerodynamic/structural dynamic system that may be used for stability analysis. The work in this paper assumes rigid structures, but does include the rigid-body degrees of freedom as states such that flight-dynamic modes may be studied.

2.3.1 Stability of the SHARP Homogeneous System

This section describes how SHARP is utilized to perform stability analysis for a given configuration. Symbolically, this process may be represented using the block diagram shown in Figure 2.
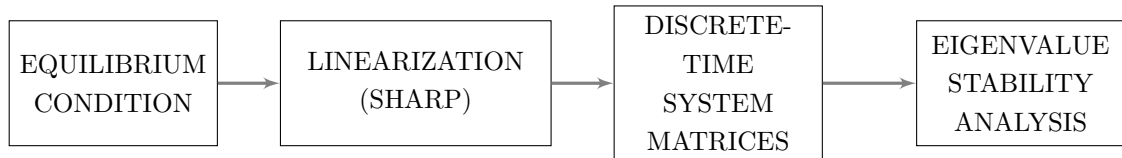

Figure 2: Flowchart describing the process for stability analysis.

From equilibrium, SHARP routines are utilized to assemble the linear system matrices. An eigenvalue problem is formulated from the system matrices, from which the eigenvalues are studied to look at modal behavior and stability. The following sections give an overview of the homogeneous system matrices and proceed to describe the stability analysis problem in detail.

2.3.2 Homogeneous System Matrices

SHARP routines are utilized to perform a linearization of the aerodynamic and rigid-body equations. Full details on the linearization are presented in Murua et. al [4]. The linearized UVLM and rigid-body equations are assembled into a unified framework with an analytical coupling between the aerodynamic and rigid-body states. The resulting system can be cast into a discrete-time state-space formulation with the form

$$E_{sys}\mathbf{\Delta} \boldsymbol{x}^{n+1} = A_{sys}\mathbf{\Delta} \boldsymbol{x}^n \tag{3}$$

where the state vector is

$$\boldsymbol{x} = \begin{bmatrix} \boldsymbol{x}_A^T \mid \boldsymbol{x}_R^T \end{bmatrix} = \begin{bmatrix} \boldsymbol{\Gamma}_b^T & \boldsymbol{\Gamma}_w^T & \dot{\boldsymbol{\Gamma}}_b^T & \mid & \nu^T & \Theta^T \end{bmatrix}^T \tag{4}$$

that describes the system completely. The full state vector concatenates the aerodynamic circulation states, the rigid-body linear and angular velocities ($\nu = \begin{bmatrix} u & v & w & p & q & r \end{bmatrix}$), and the rigid-body orientation angles ($\Theta = \begin{bmatrix} \phi & \theta & \psi \end{bmatrix}$).

The system matrices themselves may represented in a partitioned form, with entries that look like

$$E_{sys} = \begin{bmatrix} E_A & \mid & E_{A,RB} \\ \hline E_{RB,A} & \mid & E_{RB} \end{bmatrix}, \quad A_{sys} = \begin{bmatrix} A_A & \mid & A_{A,RB} \\ \hline A_{RB,A} & \mid & A_{RB} \end{bmatrix}$$

where the subscript 'A' refers to the aerodynamic model and the subscript 'RB' refers to the rigid body model. Interface terms are required to map between the two models.

2.3.3   Linearized Aerodynamic Subsystem

As this work focuses on modifying the aerodynamic model to include the effect of stall using decambering; terms in the aerodynamic subsystem are explained next. The equations that describe the aerodynamics are based on a linearized form of the UVLM equations presented in Section 2.2. Following a small-perturbation analysis, the UVLM boundary-condition equation (Equation 1) and wake-propagation equation (Equation 2), are re-cast as:

$$A_b^o \Delta \boldsymbol{\Gamma}_b^{n+1} + A_w^o \Delta \boldsymbol{\Gamma}_w^{n+1} + W_b^o \Delta \dot{\boldsymbol{\zeta}}_b^{n+1} = 0, \tag{5}$$

where the term W_b^o is used to store the vortex-ring normal vector information for the equilibrium configuration, and

$$\Delta \boldsymbol{\Gamma}_w^{n+1} = C_{\Gamma b} \Delta \boldsymbol{\Gamma}_b^n + C_{\Gamma w} \Delta \boldsymbol{\Gamma}_w^n. \tag{6}$$

A mid-point integration scheme is used for the computation of the derivative of the bound circulation as:

$$\Delta \boldsymbol{\Gamma}_b^{n+1} - \frac{1}{2} \Delta t \Delta \dot{\boldsymbol{\Gamma}}_b^{n+1} = \Delta \boldsymbol{\Gamma}_b^n + \frac{1}{2} \Delta t \Delta \dot{\boldsymbol{\Gamma}}_b^n. \tag{7}$$

The linearized UVLM Equations 5–7 partially define the aerodynamic subsystem, where the inputs are taken to be the changes in the aerodynamic lattice velocities and outputs are given as the changes in aerodynamic loads. Details regarding the linearized aerodynamic loads equations may be found in Ref. [4]. Two important features regarding the aerodynamic model implemented in the system matrices must be emphasized for the upcoming discussion in Section 2.4: (1) All terms in Equations 5–7, except for those retained as states (circulations) or as inputs (aerodynamic grid velocities), are computed only at the equilibrium condition (with these terms denoted by the 'o' superscript), and (2) there exists an analytical relationship between the inputs and outputs of the linearized aerodynamic model, such that the outputs (loads) may be computed by pre-multiplying elements of the state vector by pre-stored constant matrices, such as those in expressions 5–7, that are placed in the appropriate locations in the E_{sys} and A_{sys} matrices.

2.4   Integration of the Stall Model in SHARP for Stability Analysis

In this section, the incorporation of the decambering post-stall model into the SHARP stability-analysis framework is described. Firstly, the stall model includes the rotation of the panel normal vectors, stored in the matrix W_b^o, due to decambering required for the establishment of the reference condition. In addition, this model takes into account the effects of body-axis motion on the decambering, which alters the aerodynamic force, on each strip of the lifting surfaces. The impetus for attempting to include the effects of stall on the prediction of aerodynamic forces may be seen in discussions in References [13] and [14] regarding roll rate damping. A similar discussion, as it pertains to the problem at hand, is presented below.

Consider an aircraft undergoing a steady roll-rate, as shown in Figure 3(a). The roll rate causes an angle of attack distribution, shown in Figure 3(b), which varies linearly across the span from $pb/2u$ at the left wingtip to $-pb/2u$ at the right wingtip. Figure 3(c) shows two different wing angle of attack cases, one low and one high, at which the roll-rate effect may be considered. For the low-α case, the roll rate causes an anti-symmetric
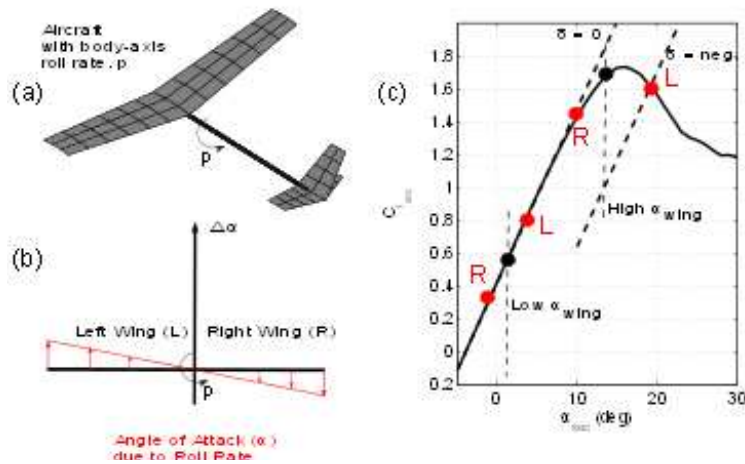
Figure 3: Aircraft undergoing steady roll rate.

increment in the angle of attack on the left and right wing. The right wing experiences a lower angle of attack and produces less lift. Conversely, the left wing experiences a higher angle of attack and a higher amount of lift production. Both wings operate in the linear regime on the C_l-α curve, and no decambering is required ($\delta_1 = 0$).The net result is that a restoring moment is created that acts to oppose the roll rate. Due to this effect, the roll rate is highly damped. Considering the high-α equilibrium case next, we have a small amount of decambering required for the potential flow prediction to converge on the viscous input data. The same anti-symmetric distribution of angle of attack is placed on the configuration due to roll rate. The right wing, experiences a lower angle of attack, and develops less lift. Although the left wing experiences a higher angle of attack, due to the nonlinearity in the C_l-α curve, the amount of lift may not necessarily increase. This behavior results in a reduction in the roll damping at the high-α condition.

Although the discussion above applies to the changes in lift behavior due to roll rate, similar changes may occur as well when variations in other body-axis velocities occur. It is desired that these changes be correctly captured in the implementation of the stall model.

2.4.1 Implementation of the Stall Model

The challenge in the implementation of this stall model is the desire for the decambering to change as motion occurs, and for the aerodynamic force to be adjusted accordingly. Initial attempts focused on including the decambering variables as states in the aerodynamic system. These attempts were unsuccessful. In order to be included as a state, there would need to exist a relationship between the decambering at time step n and time step $n + 1$, that could be written analytically. By the nature of the decambering calculation, the amount of decambering required for a given strip on a lifting surface is dependent on the strip's current operating point in the C_l-α space. Perturbing a body-axis velocity component will alter the amount of decambering present for a given strip if it is operating in the post-stall regime, but the amount that the decambering will vary is dependent on the nonlinear viscous input data. The decambering calculation relies heavily on utilizing this viscous input data as a look-up table as the post-stall iterations approach convergence. The requirement to look up viscous data to determine the change in decambering prevents relating the decambering at time step n and time step $n + 1$ analytically, which rules out including the $\Delta\delta_1$ vector as a state.

7

Rather than including the decambering vector in the states, the change in decambering is considered a control input and introduced to the system matrices as such. Considering the discrete time system from Equation 3, a control input is added as:

$$E_{sys}\Delta \boldsymbol{x}_{sys}^{n+1} = A_{sys}\Delta \boldsymbol{x}_{sys}^{n} + G_{con}\Delta \boldsymbol{u}_{con}^{n} \tag{8}$$

The control input is taken to be the change in decambering from the equilibrium condition, $\Delta \boldsymbol{\delta_1}$. The change in decambering introduced to the system, and thus the change in the amount of circulation carried by the affected panels is related to the change in the rigid-body velocities, as discussed in Section 2.4. In the local area right around the equilibrium configuration, the change in decambering is assumed to be linearly related to the change in flight velocities as

$$\Delta \boldsymbol{u}_{con}^{n} = \Delta \boldsymbol{\delta_1}^{n} = K_{dec}\Delta \nu^{n} \tag{9}$$

where

$$K_{dec} = \begin{bmatrix} \frac{\partial \delta_{1,1}}{\partial u} & \frac{\partial \delta_{1,1}}{\partial v} & \frac{\partial \delta_{1,1}}{\partial w} & \frac{\partial \delta_{1,1}}{\partial p} & \frac{\partial \delta_{1,1}}{\partial q} & \frac{\partial \delta_{1,1}}{\partial r} \\ \frac{\partial \delta_{1,2}}{\partial u} & \frac{\partial \delta_{1,2}}{\partial v} & \frac{\partial \delta_{1,2}}{\partial w} & \frac{\partial \delta_{1,2}}{\partial p} & \frac{\partial \delta_{1,2}}{\partial q} & \frac{\partial \delta_{1,2}}{\partial r} \\ \vdots & \vdots & \vdots & \vdots & \vdots & \vdots \\ \frac{\partial \delta_{1,N}}{\partial u} & \frac{\partial \delta_{1,N}}{\partial v} & \frac{\partial \delta_{1,N}}{\partial w} & \frac{\partial \delta_{1,N}}{\partial p} & \frac{\partial \delta_{1,N}}{\partial q} & \frac{\partial \delta_{1,N}}{\partial r} \end{bmatrix} \tag{10}$$

The K_{dec} matrix is computed using finite differencing between steady vortex lattice runs. Depending on whether a one-sided or central finite difference is used, this requires six or twelve vortex lattice and an equal number of decambering evaluations for each trim condition being considered. Each column of the K_{dec} matrix is filled out by varying one of the rigid-body velocity components from the equilibrium condition, transferring the motion induced velocity to the aerodynamic grid, and solving the system using the decambering iteration briefly described in Section 2.1. The gradient representing the change in decambering due to a small velocity perturbation for each strip is stored in the K_{dec} matrix, which is valid only around the equilibrium condition being studied. For pre-stall conditions, the small velocity perturbations do not move the operating points off of the linear portion of the C_l-α input curves, and all of the K_{dec} matrix entries evaluate to zero.

2.4.2 The Control Input Matrix

The control input matrix, G_{con}, is computed to introduce the effect of changing the decambering on the system matrices. The effect is introduced by taking into account the change in orientation of panel normal vectors on the non-penetration boundary condition. The main contribution of the decambering comes from the non-circulatory induced velocities, and no correction is made for the effect on influence-coefficient matrices.

With the control input defined, it is substituted into Equation 8.

$$E_{sys}\Delta \boldsymbol{x}_{sys}^{n+1} = A_{sys}\Delta \boldsymbol{x}_{sys}^{n} + G_{con}K_{dec}C\Delta \boldsymbol{x}_{sys}^{n}, \tag{11}$$

In Equation 11, the matrix C is introduced which selects the rigid-body velocities from the full state vector, as shown in Equation 12, as these are needed to compute the control input at time step n.

$$\Delta \boldsymbol{\nu}^{n} = C\Delta \boldsymbol{x}_{sys}^{n} \tag{12}$$

2.4.3   The Eigenvalue Problem for the UVLM + Decambering Stall Model

Factoring the state vector out of Equation 11 makes it clear that the discrete time eigenvalue problem for the system describing the stall model model may be written as shown in Equation 13.

$$E_{sys}\boldsymbol{v}_i = z_i[A_{sys} + G_{con}K_{dec}C]\boldsymbol{v}_i \tag{13}$$

3   Numerical Studies

Numerical studies are presented in this section for a free-to-roll wing and for a full aircraft configuration. The free-to-roll wing represents a simple test case. This simple case is found to be useful to consider, as some expectation for the roll damping behavior is known (as discussed in Section 2.4), and including only one rigid-body degree of freedom makes the problem more tractable. Further, the wing geometry and inertia properties were replicated based on an experimental campaign that produced results for roll damping even beyond the stall. The wing is studied for pre- and post-stall equilibrium conditions, and the capability of the stall-model implementation to capture the roll-damping characteristics from experimental results is examined. Subsequently, a full aircraft configuration is considered. Stability results for the full aircraft at level-flight trim conditions yield the characteristic flight dynamic modes at low angles of attack. In this regime, no post-stall model is required and the flight dynamic modes are compared to other potential flow based analysis methods. As the trim angle of attack approaches and exceeds the stall, the effects of the stall model become apparent. Qualitatively, these predictions match experimental results for aircraft flight dynamics.

3.1   Free to Roll Wing

In this section, the stability of a free-to-roll wing is considered. The free-to-roll wing is a wing geometry studied with only the roll degree of freedom active, as may be studied in a wind tunnel investigation. The full system linearization described in Section 2.4 is reduced for this study to the free-to-roll form by removing rows and columns of appropriate subsystem matrices and interface terms. This is a simpler case compared to that of a full aircraft, and one where roll damping results are available for comparison from References [15, 16].

The wing geometry comes from a Schweizer SGS 1-36 sailplane, with an aspect ratio of 15, and Wortmann airfoil sections. The wing is modeled in the vortex lattice using the FX 61-163 airfoil for the camberline shape across the entire span, and a nondimensional time step of $\Delta t^* = V_\infty \Delta t/c = 0.25$, where c is the characteristic chord length, and discretized using 4 panels chordwise and 20 panels spanwise. The geometry is shown in Figure 4a, with relevant geometric and mass properties of the wing in Table 1. The input viscous airfoil information, required by decambering, is shown in Figure 4b. The viscous input data shown in Figure 4b were generated by relying on three sources: (1) XFOIL [17] was used to generate viscous C_l input information up to $C_{l_{max}}$, (2) experimental data for the Wortmann series airfoils was consulted to accurately reproduce the immediate post-stall behavior [18], and (3) characteristic lift coefficient behavior was input beyond the range covered by the airfoil experimental data. The characteristic behavior comes from CFD studies that were carried out by this author and colleagues [19]. These CFD studies show that even for airfoils with vastly different behavior in the region immediately

after stall, the C_l-α curves nearly coincide eventually, paticularly in the deep-stall region. Further, making this assumption is consistent with aerodynamic models proposed for airfoil aerodynamics beyond stall proposed by Lindenburg [20] and Viterna [21].

Table 1: Geometric Properties for the Free-to-Roll Wing

Geometry	Main wing	Reference Data	
Span	14 m	Mass	82.6 kg
Root Chord	1.28 m	I_{xx}	1,345 kg-m^2
Tip Chord	0.576 m	S_{ref}	13 m^2
Dihedral	0 deg	b_{ref}	14 m
Airfoil Cross Section	FX 61-163	c_{ref}	1 m
Viscous Input Data	C_l		

(a)   (b)
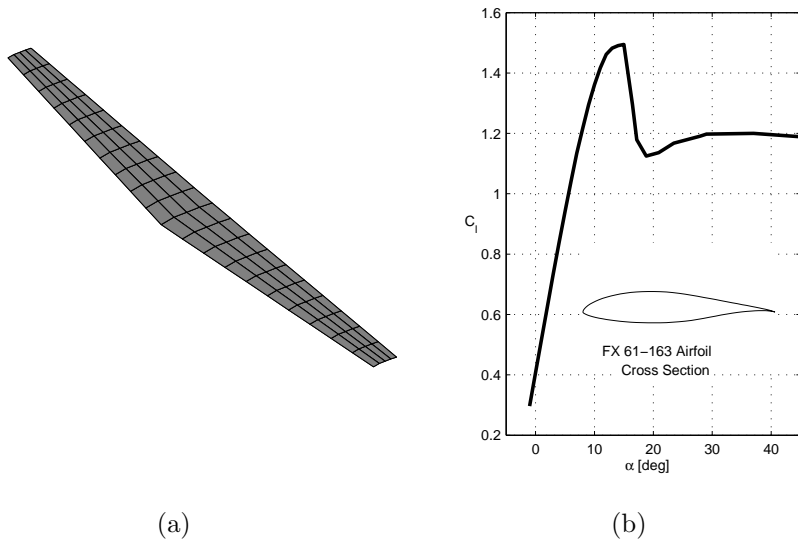
Figure 4: The free-to-roll wing configuration: (a) isometric view, and (b) input viscous airfoil C_l-α information. The airfoil cross section is shown in the inset.

Following definition of the lifting surfaces in the vortex-lattice environment, equilibrium conditions are established for a range of angles of attack using the VLM + decambering. The cases studied used a freestream velocity of 10 m/s and $1 \leq \alpha \leq 40$ degrees. Next, SHARP (modified with the stall models) was used to perform the linearization and stability analysis on the free-to-roll system. The raw results from SHARP consist of the real pole which corresponds to the dimensional roll damping derivative, denoted L_p.

For comparison purposes the dimensional roll damping values output from the stability analysis are converted to a non-dimensional form, C_{lp}, through the relationship in Equation 14,

$$C_{lp} = \frac{2QI_{xx}}{\bar{q}Sb^2}L_p \qquad (14)$$

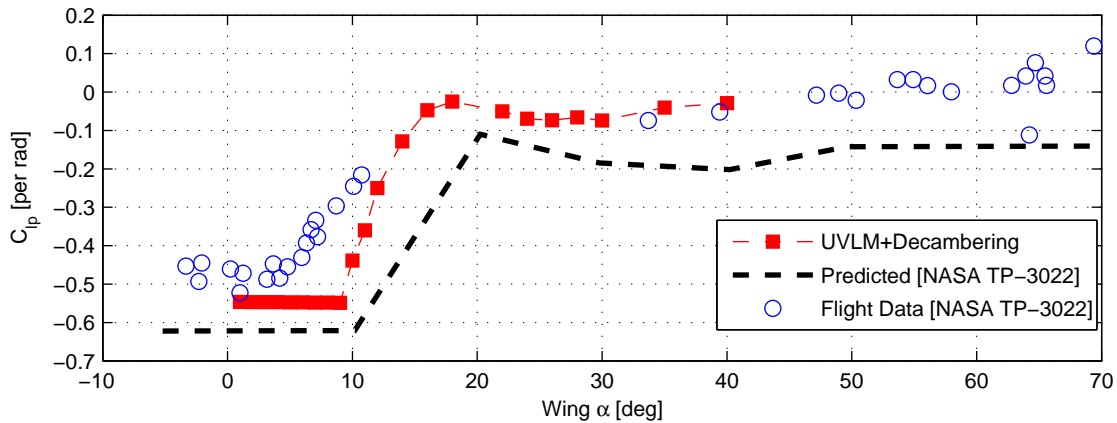where Q is the freestream speed and $\bar{q}$ is the dynamic pressure.

10

Figure 5: Variation of non-dimensional roll-damping derivative with increase in the wing angle of attack. Comparison data is from Ref. [15]

Figure 5 presents the non-dimensional roll damping results from the UVLM implementations as well as the results by Sim in References [15] and [16]. Sim presents two sets of results for the non-dimensional roll damping coefficient — predicted and from flight test. In the results of [15], there is a discrepancy between the predicted and flight-test roll damping derivative, with the flight-test data showing significantly less damping than the predicted values, and the onset of reduction of the damping coefficient (in absolute value) occurring at a lower angle of attack. It is noted, however, that the two methods show consistent trends. For $12 \leq \alpha \leq 34$ degrees, flight test data is not reported, although a predicted value of roll damping is provided. At low angles of attack, the stall model implemented in SHARP gives the same results for the roll damping coefficient as is seen using a purely potential flow analysis method, which is to be expected. As the angle of attack is increased to 10 degrees, the stall model results begin to show a loss of roll damping. Beyond 10 degrees, the roll damping predicted by the stall model continues to move towards the stability boundary until it essentially settles at a very small, but still negative, value.

Good agreement is seen between the results of [15] and the UVLM+ decambering stability prediction methodologies at low angles of attack, with the low-order prediction method falling between the predicted and experimental results of [15]. As the wing begins to stall around 10 degrees angle of attack, the need for the stall model comes to light. Not only does the stall model predict the loss of roll stability, but it shows the roll stability progressing from very stable to abutting against the stability boundary over very nearly the same wing angle-of-attack range as the NASA TP data. Further, the quantitative values of roll damping at high-α from the stall model agree very well with the flight test data. The stall model appears very capable of capturing the salient effects on the rolling dynamics as the angle of attack is increased through and even well beyond stall. Further, these results suggest that the model form chosen, of taking the change in decambering being linearly related to the change in flight velocities, is appropriate to the problem at hand.

3.2   Full-Aircraft Stability Results

A full-aircraft configuration with external geometry, weights, and inertias similar to a commercial UAS is studied in this section. The first challenge working towards examining

the stability and flight dynamic characteristics of such a configuration is to arrive at an trim condition about which to perform the linearization and stability analysis. The test case is described in Section 3.2.1, trimming is covered in Section 3.2.2, and results are presented in Section 3.2.3.

3.2.1 Test Case

The aircraft studied is shown in Figure 6(a) with details of the geometry, weights, and inertias in Table 2. Viscous airfoil input information representing the NACA 4415 airfoil from CFD from Reference [19] shown in Figure 6(b), is applied to the main wing of the configuration, while the tail surfaces are assumed to operate in purely potential flow. The aircraft consists of a main wing with a moderately large aspect ratio and a small amount of dihedral to enhance directional stability, and a conventional horizontal and vertical tail. The entire horizontal tail plane acts as a control surface, making it a stabilator. The propulsive thrust acts along the body-axis X direction. All numerical studies using the vortex lattice aerodynamics use a nondimensional time step of $\Delta t^* = V_\infty \Delta t / c = 0.25$ where c is the characteristic chord length. The main wing is discretized using 4 panels chordwise and 12 panels spanwise. The tail surfaces have a shorter chord than the main wing and as such are discretized using 3 panels chordwise with 8 total spanwise panels across the horizontal tailplane and 4 spanwise panels on the vertical tailplane.

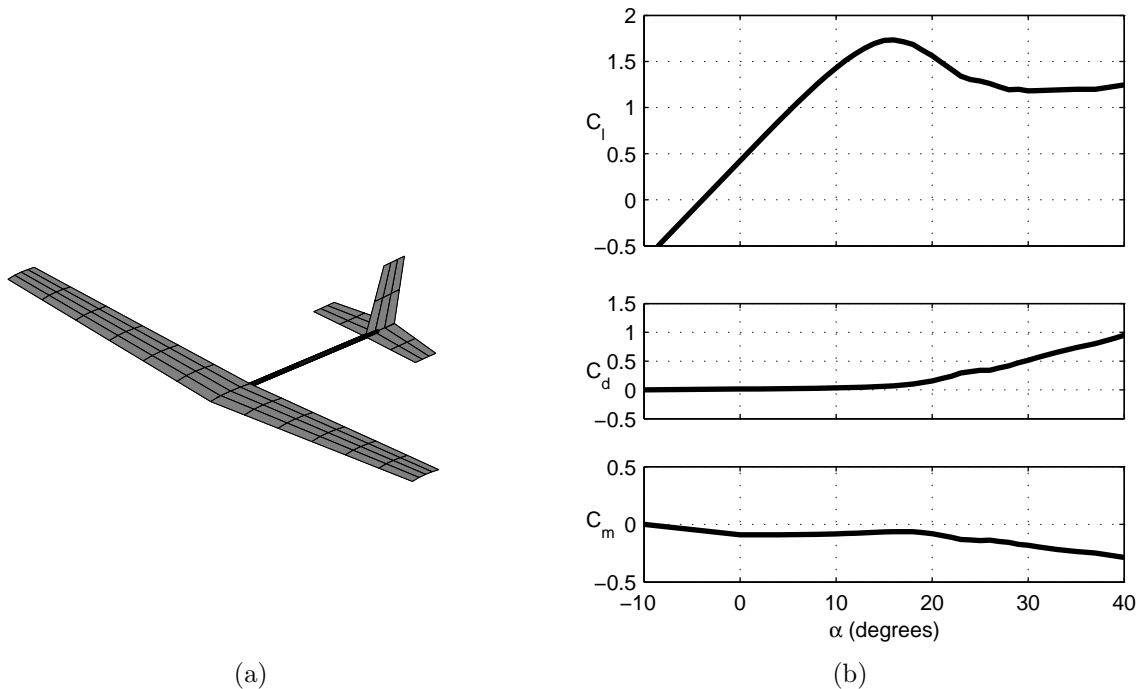

(a)   (b)

Figure 6: The configuration for the full-aircraft stability test case: (a) Isometric view of the aircraft, and (b) Viscous airfoil input information applied to the main wing.

Table 2: Aircraft geometric properties, inertial properties, and reference information for the configuration used in the full aircraft used for stability results.

Geometry	Main wing	HTP	VTP
Span	2.8 m	0.7 m	0.35 m
Root Chord	0.27 m	0.2 m	0.2 m
Tip Chord	0.18 m	0.14 m	0.14 m
Dihedral	5 deg	0 deg	–
Airfoil Cross Section	NACA 4415	Symmetric	Symmetric
Viscous Input Data	C_l, C_d, C_m	None	None
Aircraft Reference Data	Mass	8.6 kg	
I_{zz}	1.78 kg-m^2	I_{xx}	1.64 kg-m^2
S_{ref}	0.63 m^2	I_{yy}	0.54 kg-m^2
b_{ref}	2.8 m	c_{ref}	0.225 m

3.2.2 Trim Calculation

An aircraft is considered as trimmed when it is following a steady level flight trajectory in the absence of external disturbances. The level-flight trajectory is enforced by constraining the pitch orientation angle and freestream aircraft angle-of-attack to be equal. The trim cases studied all require zero sideslip and zero angular velocities. With these conditions enforced, and by providing symmetric initial conditions for the decambering vector δ_1 for surfaces on the port and starboard sides of the aircraft, the resultant aerodynamic loads, computed either in purely potential flow or those modified by decambering, remain symmetric laterally. Therefore, only longitudinal trim is needed. This trimming is done by fixing the free-stream angle of attack, α, by providing trim inputs for the elevator deflection, δ_e, thrust, T, and free-stream speed, Q. Trim iterations follow a standard Newton-Raphson method and are described by the flowchart in Figure 7. Given initial guess trim input variables, the aerodynamics are evaluated using the vortex lattice method including decambering iterations run to convergence when required. The total vertical force, horizontal force, and pitching moment are computed. If the residual force and moment have been driven below a pre-defined tolerance, trim is considered to have been established and the current values of the trim variables are saved. If not, subiterations are run to establish a relationship between the trim inputs and the changes in horizontal force, vertical force, and pitching moment. Each subiteration consists of an evaluation of the configuration aerodynamics using VLM + decambering when a small change has been applied to a trim input variable. The output change in horizontal and vertical force and pitching moment due to a change in trimming variable are assembled into Jacobian matrix, from which the new guess values of trim inputs are computed. The routine repeats until trim is achieved.

In pre-stall cases, where no aerodynamic non-linearities due to flow separation occur, the trim routine converges very rapidly (three to four iterations are generally sufficient) even when the initial guess values are poor. More iterations are required when the aerodynamic solution requires decambering, and generally convergence is reached in less than 20 iterations without the need for relaxation. Figure 8 shows the trimmed aircraft in a low- and high-α_{AC} condition. At a low α_{AC}, the aircraft pitch angle is very low, all the sectional operating points on the main wing fall on the linear portion of the input C_l-α
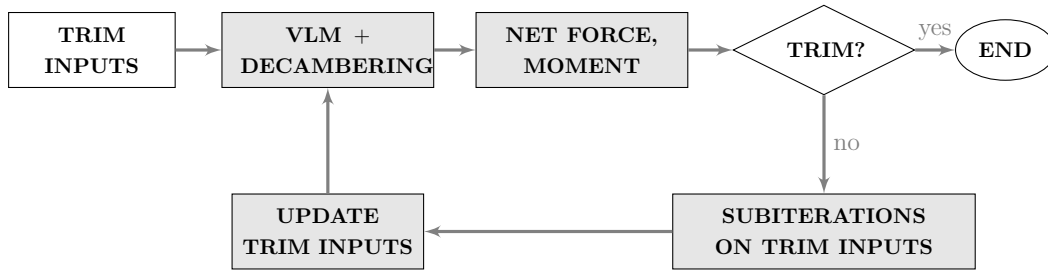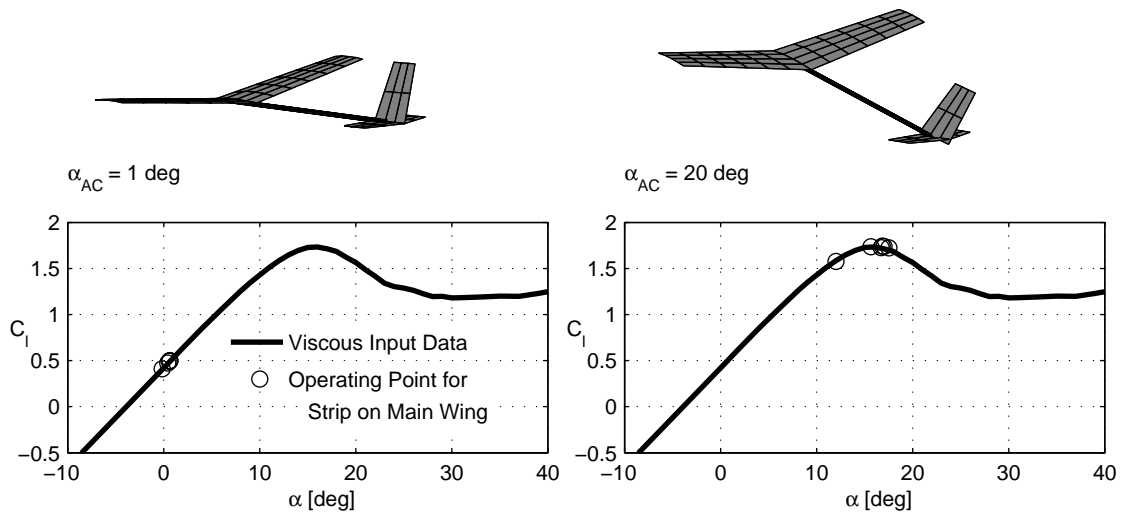
Figure 7: Trimming routine outline.

Figure 8: Aircraft orientation and operating points for the main wing strips shown for $\alpha = 1$ deg (left) and $\alpha = 20$ deg (right).

curve, and no decambering is required. For the high α_{AC}, the aircraft pitch angle is high, decambering is required during the trim iterations, and the main wing operating points fall on the non-linear portion of the C_l-α curve.

Figure 9 shows the freestream speed, elevator deflection, and thrust required to trim the aircraft for $\alpha_{AC} = 1$ through 24 degrees. As the α_{AC} is increased, the trim speed for the aircraft initially becomes lower until some minimum is reached. The minimum speed corresponds to the maximum lift coefficient that may be developed by the aircraft. Beyond the maximum configuration C_L, as portions of the main wing begin to stall, the trim speed actually must increase to satisfy the trim requirement of steady level flight. A substantial contribution to the pitching moment moment comes from the horizontal tail plane. As the angle of attack of the aircraft is increased, more stabilator deflection is required to maintain trim. At low α_{AC}, little thrust is required to overcome drag and maintain steady flight. As the angle of attack is increased, both the induced and profile drag increase, necessitating additional thrust to maintain level flight. A rapid rise in thrust required is seen after the stalling angle of attack is exceeded due to the much larger amount of induced and profile drag acting on the lifting surfaces beyond stall.
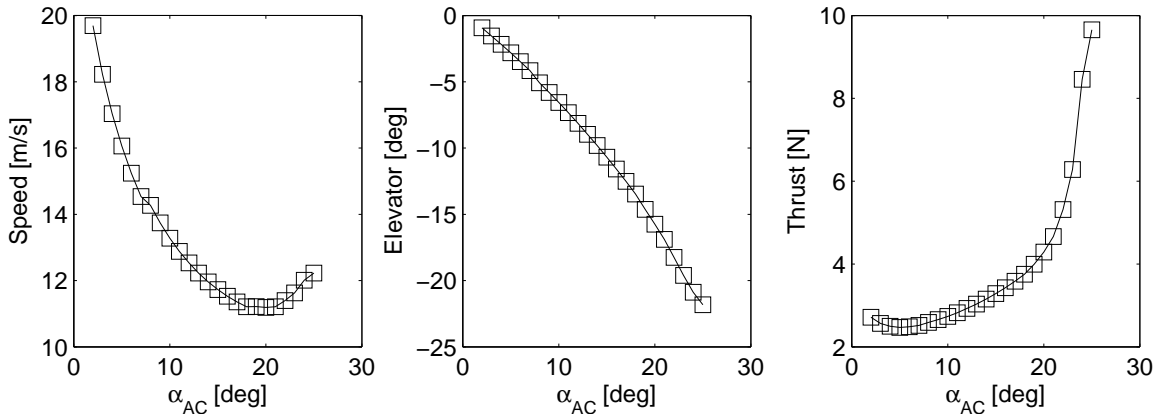
Figure 9: Trim solutions for $1 \leq \alpha_{AC} \leq 25$ degrees.

3.2.3 Stability Results

Once the trim conditions have been determined, the linearization and stability analysis (Section 2.4.3) may be carried out. The stability analysis gives as many eigenvalues as the system has states and will include both lateral and longitudinal modes. The rigid body modes are identified by sorting the continuous-time eigenvalues of the system and examining the shape of the corresponding eigenvectors. As the rigid-body modes typically appear in the first 15 eigenvalues when sorted by magnitude, manual interpretation is kept to a minimum.

At low angles of attack, the continuous-time eigenvalues that describe the dynamic modes for the aircraft as predicted by the UVLM + decambering stall model may be compared with other potential-flow analysis methods (such as the Athena Vortex Lattice (AVL) code, Ref. [22]), as no stall model is needed. Unlike SHARP, the stability analysis in AVL retains only the flight velocities and orientation angles as states, and therefore the stability results themselves are easier to interpret. Comparison with the AVL results serves to verify that SHARP is producing reasonable results and also checks that the eigenvalues that are being chosen to describe the aircraft stability characteristics are indeed the rigid-body modes. This comparison is only valid in attached flow conditions, and as such the results from AVL are not plotted for the full range of α.

For clarity, the stability results are presented separately for the longitudinal and lateral-directional modes. Figure 10 shows a root locus of the longitudinal modes as angle of attack is increased. Stall model results are presented for the range $2 \leq \alpha \leq 25$ degrees. Results from AVL analysis are presented for $2 \leq \alpha \leq 10$ degrees. Four branches appear on the root locus. These branches correspond to four characteristic longitudinal modes of a rigid aircraft. Except for the very high angle-of-attack cases predicted by the stall model, these modes are manifested as two pairs of complex conjugate roots: one with high frequency and high damping and the other with low frequency and low damping.

The high-frequency pair of eigenvalues is associated with the short-period mode. At low angles of attack, the short-period is highly damped, and excellent agreement is seen between the stall model and AVL, an example of which is highlighted in Table 3 for $\alpha = 2$ degrees. As the angle of attack is increased and the trim speed decreases, the stall model and AVL results predict a decrease in damping along with a modest decrease in natural frequency. AVL predicts the short-period frequency and damping decreasing
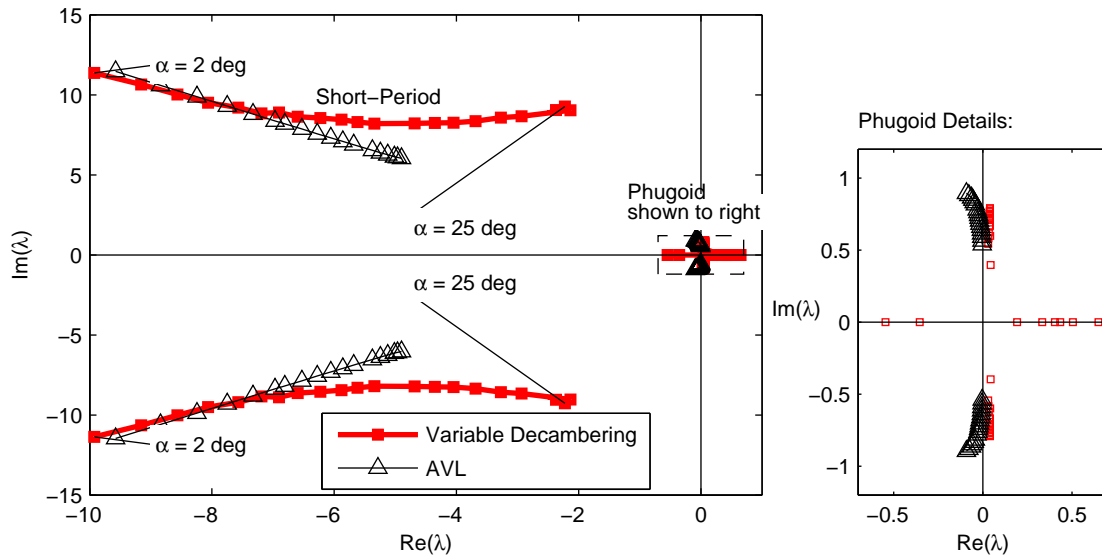
15

Figure 10: Variation of the eigenvalues for the longitudinal modes with increase in angle of attack.

Table 3: Longitudinal continuous-time eigenvalues compared to other analysis method.

$\alpha = 2$ deg.			
Short-Period (UVLM)	$-9.92 \pm 11.36i$	Phugoid (UVLM)	$0.0296 \pm 0.54i$
Short-Peroid (AVL)	$-9.57 \pm 11.46i$	Phugoid (AVL)	$-0.0039 \pm 0.54i$

nearly linearly up to the maximum angle of attack for which it is plotted (10 degrees). Considering the UVLM + decambering stall model, beyond the maximum configuration C_L, increasing the angle of attack has little effect on the natural frequency, but the damping drops (in absolute value) sharply.

The low-frequency pair of eigenvalues corresponds to the phugoid mode of the aircraft. These eigenvalues are located very close to the origin in Figure 10, and are shown in an expanded view in the figure inset in order to aid the interpretation. For the 2-degree angle-of-attack case, these are compared to the AVL results in Table 3. Both the stall model and AVL resutls show the phugoid roots to have very low (absolute values) damping, and the agreement in frequency is exceptional. It is noted, however, that although the damping for each prediction method is small, the UVLM and AVL predictions show the phugoid on opposite sides of the imaginary axis, meaning that AVL predicts the phugoid to be slightly stable while the UVLM predicts the phugoid to be slightly unstable. The degree of instability predicted by the UVLM is small and it is possible to have an aircraft that is statically stable but with an undamped phugoid oscillation [23]. The disagreement between the two analysis methods is not well understood at this time although plausible reasons for it include how the drag is modeled in AVL and UVLM and the fact that thrust is included in the trim calculation for the UVLM model, but not with the AVL model. Despite the discrepancy in the predicted damping values for the phugoid mode, the trend that is exhibited as the trim speed decreases (and angle of attack increases) is the same for both the UVLM and AVL predictions. As the angle of attack is increased, the damping of the phugoid mode remains relatively unchanged while the natural frequency increases. Beyond the maximum configuration C_L, the stall model begins to predict two
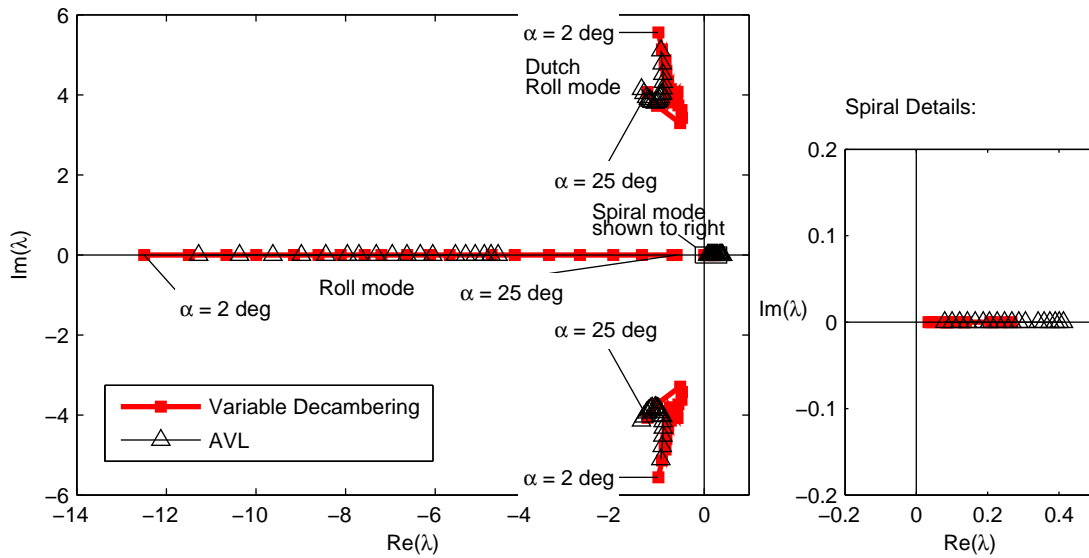
Figure 11: Variation of the eigenvalues for the lateral modes with increase in angle of attack.

zero-frequency longitudinal modes. These modes occur after the wing is nearly fully stalled.

The trends shown by the longitudinal eigenvalues as the trim angle of attack is increased are shown to be the same for the UVLM predictions and AVL in the low angle of attack range. Beyond stall, however, the AVL comparison is no longer valid (and thus not plotted). Further, the longitudinal modal characteristics are not necessarily intuitively predicted as the stalling angle of attack is approached and exceeded. The stall model implemented in the SHARP stability analysis offers a prediction in this range but the validity of the prediction is not well vetted. The trends displayed by the stall model, however, may be compared qualitatively to results presented by Stengel and Nixon [24], who studied the longitudinal flight dynamic characteristics for a general aviation aircraft as stall is approached. In results of [24], the short-period frequency and damping decrease as the speed is reduced, until the minimum power point is reached. At angles of attack beyond the minimum power point, particularly as the stall is approached, the natural frequency of the phugoid mode is nearly constant and the damping drops dramatically. Synchronously, the phugoid natural frequency is shown to increase while the damping remains nearly constant. While not enough configuration information was available from the Stengel report to reproduce the configuration and results, the trends align quite well with the predictions provided by the UVLM + decambering stall model.

The continuous time eigenvalues describing the lateral-directional modes of the aircraft are plotted in a root-locus in Figure 11. Four branches of the root locus are shown, with results presented from AVL for $2 \leq \alpha \leq 10$ degrees, and the UVLM + decambering stall model for $2 \leq \alpha \leq 25$ degrees. The four branches correspond to three characteristic modes of a rigid aircraft.

At low angles of attack, there is a very highly damped zero-frequency mode, aligned most closely with the roll degree of freedom of the aircraft. At $\alpha = 2$ degrees, the roll mode from UVLM + decambering is compared against the AVL prediction in Table 4. The predictions from the two methods are in good agreement, with approximately a 10%

Table 4: Lateral-directional continuous-time eigenvalues compared to other analysis method.

	$\alpha = 2$ deg.
Roll Damping (UVLM)	-12.50
Roll Damping (AVL)	-11.30
Spiral (UVLM)	0.034
Spiral (AVL)	0.079
Dutch Roll (UVLM)	$-1.02 \pm 5.56i$
Dutch Roll (AVL)	$-0.97 \pm 5.11i$

difference. As the angle of attack is increased, the damping of the roll mode decreases in the AVL predictions as well as in the stall model. The reduction in roll damping is much more pronounced in the stall model.

The other zero-frequency mode corresponds to the spiral mode of the aircraft. At 2-degree angle of attack, the spiral mode is predicted to be unstable by the UVLM method and AVL. This mode is located very close to the origin on the root locus, and as such is shown on the inset in Figure 11. As the angle of attack is increased, the spiral mode becomes more unstable as predicted by both modified UVLM and AVL. The degree of instability is relatively close in all three analysis methods, and hence not affected by stall, it appears.

The final mode plotted for the lateral-directional stability results is a complex conjugate pair, called the dutch roll mode. For the 2-degree angle-of-attack case, the UVLM and AVL predictions are compared in Table 4. The agreement between the AVL and UVLM model is excellent at low angles of attack. As the angle of attack is increased, both models predict that the dutch-roll damping remains nearly the same, and the natural frequency decreases until the maximum configuration C_L is reached. Beyond the maximum configuration C_L, the damping is shown to increase slightly.

At low angles of attack, the SHARP stability results for the lateral-directional modes compare favorably with the AVL predictions. Additional confirmation that the results are correct comes from the observation that as the angle of attack is increased, the stability predictions from SHARP and AVL move in the same manner. At high angles of attack, the roll-mode damping predicted by the stall model moves much closer to the stability boundary as compared to the AVL predictions. Qualitatively, the very lightly damped roll mode seen in the model matches the behavior of the results of the free-to-roll wing from Section 3.1 which were corroborated with experiment.

4 Conclusions

An unsteady vortex lattice method has been extended to handle stall and post-stall conditions by the incorporation of an iterative decambering approach to model boundary-layer separation on the sections of the lifting surfaces. In the stall model, a decambering-angle variable is associated with each strip of the wings/tails, which essentially controls the rotation of the strip normal vector in the vortex lattice method. Thus, the decambering variable lends itself to being incorporated as a control effector for each strip. By iteratively adjusting the decambering variables for all the strips, the aerodynamic operating point of each strip is made to coincide with the input viscous lift curve for the airfoil section even

at post-stall conditions, while the vortex lattice boundary conditions are simultaneously satisfied. With this coupling of a vortex lattice method with a stall model, a modeling environment has been developed for analysis of rigid-aircraft flight dynamics in pre- and post-stall conditions, with capability for future extensions to include structural flexibility.

The current capabilities include trim calculations, linearization of the aircraft dynamics equations about the trim condition to yield a state-space form, and eigenvalue analysis to determine stability characteristics of the aircraft in both pre- and post-stall conditions. Of particular interest is the state-space form of the equations, in which decambering is introduced into the system matrices as a control effectors whose values are linearly related to changes in the flight velocities. This relationship between flight-velocity changes and decambering changes is appended to the system matrix in feedback form, allowing for eigenvalue analysis of the augmented system matrix for stability analysis even in post-stall conditions. Results from the model for roll stability of a sailplane wing agrees excellently with flight tests results, showing loss of roll damping with increasing angle of attack. Full-aircraft results for all flight modes agree well with another analysis method for pre-stall conditions. At post-stall conditions, the full-aircraft predictions are in broad agreement with general trends in the literature.

5   Acknowedgments

References

[1] Su, W. and Cesnik, C. E. S., "Dynamic Response of Highly Flexible Flying Wings," *AIAA Journal*, Vol. 49, No. 2, February 2011, pp. 324–339.

[2] Patil, M. J., Hodges, D. H., and Cesnik, C. E. S., "Nonlinear Aeroelasticity and Flight Dynamics of High-Altitude Long-Endurance Aircraft," *Journal of Aircraft*, Vol. 38, No. 1, 2001, pp. 88–94.

[3] Wang, Z., Chen, P. C., Liu, D. D., and Mook, D. T., "Nonlinear-Aerodynamics/Nonlinear-Structure Interaction Methodology for a High-Altitude Long-Endurance Wing," *Journal of Aircraft*, Vol. 47, No. 2, 2010, pp. 556–566.

[4] Murua, J., Palacios, R., and Graham, J. M. R., "Applications of the Unsteady Vortex-Lattice Method in Aircraft Aeroelasticity and Flight Dynamics," *Progress in Aerospace Sciences*, Vol. 55, 2012, pp. 46–72.

[5] Patil, M. J., Hodges, D. H., and S. Cesnik, C. E., "Nonlinear aeroelastic analysis of complete aircraft in subsonic flow," *Journal of Aircraft*, Vol. 37, No. 5, 2000, pp. 753–760.

[6] Tang, D. and Dowell, E. H., "Experimental and Theoretical Study on Aeroelastic Response of High-Aspect-Ratio Wings," *AIAA Journal*, Vol. 39, No. 8, August 2001, pp. 1430–1441.

[7] Murua, J., Martínez, P., Climent, H., van Zyl, L. H., and Palacios, R., "T-tail flutter: Potential-flow modelling, experimental validation and flight tests," *Progress in Aerospace Sciences*, Vol. 71, 2014, pp. 54–84.

[8] Mukherjee, R. and Gopalarathnam, A., "Poststall Prediction of Multiple-Lifting-Surface Configurations Using a Decambering Approach," *Journal of Aircraft*, Vol. 43, No. 3, May–June 2006, pp. 660–668.

[9] Paul, R. and Gopalarathnam, A., "Iteration schemes for rapid post-stall aerodynamic prediction of wings using a decambering approach," *International Journal for Numerical Methods in Fluids*, Vol. 76, No. 4, 2014, pp. 199–222.

[10] Katz, J. and Plotkin, A., *Low-Speed Aerodynamics*, Cambridge Aerospace Series, Cambridge University Press, 2nd ed., 2001.

[11] Murua, J., Palacios, R., and Graham, J. M. R., "Assessment of Wake-Tail Interference Effects on the Dynamics of Flexible Aircraft," *AIAA Journal*, Vol. 50, No. 7, July 2012, pp. 1575–1585.

[12] Murua, J., *Flexible-Aircraft Dynamics with a Geometricallly-Nonlinear Description of the Unsteady Aerodynamics*, Ph.D. thesis, Imperial College London, 2012.

[13] Etkin, B. and Reid, L. D., *Dynamics of Flight: Stability and Control*, John Wiley & Sons, Inc., 1996.

[14] Pamadi, B., *Performance, Stability, Dynamics, and Control of Aeroplanes*, American Institute of Aeronautics and Astronautics, 2nd ed., 2004.

[15] Sim, A., "Flight Characteristics of a Modified Schweizer SGS 1-36 Sailplane at Low and Very High Angles of Attack," NASA Technical Paper TP-3022, August 1990.

[16] Sim, A., "Flight Characteristics of a Manned, Low-Speed, Controlled Deep Stall Vehicle," NASA Technical Memorandum TM-86041, August 1984.

[17] Drela, M., "XFOIL: An Analysis and Design System for Low Reynolds Number Airfoils," *Low Reynolds Number Aerodynamics*, edited by T. J. Mueller, Vol. 54 of *Lecture Notes in Engineering*, Springer-Verlag, New York, June 1989, pp. 1–12.

[18] Selig, M. S., Guglielmo, J. J., Broeren, A. P., and Giguère, P., *Summary of Low-Speed Airfoil Data, Vol. 1*, SoarTech Publications, Virginia Beach, Virginia, 1995.

[19] Petrilli, J., Paul, R., Gopalarathnam, A., and Frink, N., "A CFD Database for Airfoils and Wings at Post-Stall Angles of Attack," AIAA Paper 2013-2916, June 2013.

[20] Lindenburg, C., "Aerodynamic Airfoil Coefficients at Large Angles of Attack," IEA Symposium Paper ECN-RX–01-004, 2001.

[21] Tangler, J., "Insight into Wind Turbine Stall and Post-stall Aerodynamics," *Wind Engineering*, Vol. 7, 2004, pp. 247–260.

[22] M. Drela and H. Youngren, "AVL Documentation," http://web.mit.edu/drela/Public/web/avl/avldoc.txt, Accessed August 2013.

[23] Federal Aviation Administration, "Flight Test Guide for Certification of Part 23 Airplanes," FAA Advisory Circular, 2003.

[24] Stengel, R. and Nixon, W., "Stalling Characteristics of a General Aviation Aircraft," *Journal of Aircraft*, , No. 82-4150, June 1982, pp. 425–434.